

Designing Xenon with Two-Dimensional Triangular Lattice

Xu Duan

Fudan University, Shanghai 200433, China

School of Science, Westlake University,

Hangzhou, Zhejiang 310024, China and

Institute of Natural Sciences, Westlake Institute for Advanced Study,

Hangzhou, Zhejiang 310024, China

Zhao Liu

Hefei National Laboratory for Physical Sciences at the Microscale,

University of Science and Technology of China, Hefei, Anhui 230026, China

School of Science, Westlake University,

Hangzhou, Zhejiang 310024, China and

Institute of Natural Sciences, Westlake Institute for Advanced Study,

Hangzhou, Zhejiang 310024, China

Brendan M Hanrahan

Sensors & Electron Devices Directorate, U.S. Army Research Laboratory,

Adelphi, Maryland 20783, United States.

Wei Zhu and Shi Liu*

School of Science, Westlake University,

Hangzhou, Zhejiang 310024, China and

Institute of Natural Sciences, Westlake Institute for Advanced Study,

Hangzhou, Zhejiang 310024, China

Abstract

Xenes, graphene-like two-dimensional (2D) monoelemental crystals with a honeycomb symmetry, have been the focus of numerous experimental and theoretical studies. In comparison, single-element 2D materials with a triangular lattice symmetry have not received due attention. Here, taking Pb as an example, we investigate the triangular-lattice monolayer made of group-IV atoms employing first-principles density functional theory calculations. The flat Pb monolayer supports a mirror-symmetry-protected spinless nodal line in the absence spin-orbit coupling (SOC). The introduction of an out-of-plane buckling creates a glide mirror, protecting an anisotropic Dirac nodal loop. Both flat and buckled Pb monolayers become topologically trivial after including SOC. A large buckling will make the Pb sheet a 2D semiconductor with symmetry-protected Dirac points below the Fermi level. The electronic structures of other group-IV triangular lattices such as Ge and Sn demonstrate strong similarity to Pb. We further design a quasi-3D crystal PbHfO_2 by alternately stacking Pb and 1T-HfO₂ monolayers. The new compound PbHfO_2 is dynamically stable and retains the properties of Pb monolayer. By applying epitaxial strains to PbHfO_2 , it is possible to drive an insulator-to-metal transition coupled with an anti-ferroelectric-to-paraelectric phase transition. Our results suggest the potential of the 2D triangular lattice as a complimentary platform to design new type of broadly-defined Xenes.

I. INTRODUCTIONS

Since the discovery of monolayer graphene and its demonstrated superb electrical, thermal, and mechanical properties, two-dimensional (2D) materials have attracted tremendous attention, driven by their potential applications for high-performance electronics^{1,2}. The atomic thickness of 2D materials is advantageous for device scaling as well as energy efficiency by lowering the operating voltage³. Distinct from 3D (bulk) materials, the surface of 2D materials does not suffer from dangling bonds, rendering them great flexibility to build up van der Waals (vdW) heterostructures in a highly controlled fashion less impacted by lattice mismatching. Moreover, vdW heterostructures can exhibit emergent phenomena that are absent in the constituent 2D materials, offering a rich platform to create and manipulate novel physical and chemical properties⁴⁻⁸.

The family of 2D materials has expanded considerably since the exfoliation of graphene via the Scotch tape technique⁹, now including materials systems possessing diverse electrical properties ranging from metals and semiconductors to wide-bandgap insulators^{10,11}. Such remarkable versatility opens up the opportunity for the design and development of flexible, ultrathin electronics. Notable 2D systems are graphene, black phosphorus, transition-metal dichalcogenides such as MoS₂, and hexagonal-BN (h-BN), which are the subjects of extensive investigations¹²⁻¹⁸. First-principles-based high-throughput calculations have identified thousands of exfoliable compounds, offering useful guidelines for experimental synthesis of new 2D systems^{19,20}. Roy *et al.* recently built a field-effect transistor with only 2D materials, using MoS₂ as the channel material, h-BN as the top-gate dielectric, and graphene as the source/drain and the contacts²¹.

The graphene-like single-element 2D materials referred to as Xenes hold an important place in the 2D family²². After the discovery of graphene, it was only natural to explore the possibility of fabricating honeycomb-lattice monolayers consisted of other group-IV elements. Given the dominant role of silicon in the electronics industry, one major technology driver for the Xene development is to enable field-effect transistors based on silicene, the silicon-based analogue of graphene²³⁻²⁶. More recently, Kane and Mele pointed out that the intrinsic spin-orbit coupling (SOC) of carbon atoms, albeit weak, opens a tiny gap in the band structure of graphene, converting the system from a Dirac semimetal to a 2D topological insulator (TI) with quantum spin hall (QSH) effect characterized by counter-propagating edge currents

with opposite spins²⁷. However, the small band gap ($\approx 10^{-3}$ meV) in graphene²⁸ makes it difficult to take advantage of the helical conducting edge states for spintronic applications. Xenes made of heavy group-IV atoms with strong SOC effects are therefore promising candidates for room-temperature QSH insulators²⁹. To date, all group-IV Xenes (silicene, germanene, stanene, and plumbene) have been synthesized experimentally^{23,30-35}. Different from graphene which is ideally flat, Xenes based on Si, Ge, Sn or Pb atoms exhibit buckled hexagonal honeycomb structures in their most stable forms. Interestingly, only plumbene is predicted to be a trivial insulator instead of a 2D TI, though the nontrivial topological states can emerge through electron doping³⁶⁻³⁸. It is noted that the concept of Xenes has become more general²², now also referring to monoelemental 2D sheets comprised of elements around group IV such as borophene^{39,40}, phosphorene⁴¹, bismuthene⁴², gallenene⁴³, and arsenene⁴⁴.

Given the supreme status of graphene in 2D material research, it is not surprising that most studies on single-element 2D systems focused on the honeycomb lattice. In comparison, 2D monolayers with the triangular lattice symmetry was much less explored. Recent studies nevertheless highlighted the potential of 2D triangular lattices to host new topological quantum states beyond 2D TIs. Zhang *et al.* predicted the presence of “destructive interference effect” between topological states in 2D triangular lattices with a tight-binding model⁴⁵. Feng *et al.* reported the presence of 2D Dirac nodal-line fermions in monolayer Cu_2Si where Cu and Si atoms are arranged in a triangular lattice⁴⁶. Another example is the non-centrosymmetric bulk compound PbTaSe_2 in which the triangular-lattice Pb monolayer plays an important role for the emergence of Weyl nodal lines in the presence of SOC⁴⁷. Notably, the 2D superconductivity was observed in a single layer of Pb grown on a Si(111) substrate, and the Pb atoms form a distorted triangular lattice^{48,49}.

In this work, we focus on 2D triangular lattices consisted of group-IV elements. Using first-principles density functional theory (DFT) calculations, we start by examining the electronic structures of a generic model: a single layer of Pb atoms arranged in a triangular lattice. It is found that the flat Pb monolayer supports a spinless nodal line in the absence of SOC while it becomes a trivial semimetal when the effect of SOC is taken into account. Interestingly, buckled Pb monolayer can also host a glide-mirror-protected nodal line in the absence of SOC. With SOC, the system becomes fully gapped and the gap size depends strongly on the degree of buckling. We further design a new compound PbHfO_2 by alternately stacking Pb and 1T- HfO_2 2D sheets. The obtained quasi-3D crystal is dynamically

stable and largely retains the electronic properties of Pb monolayers. By applying epitaxial strains to PbHfO_2 , it is possible to drive an insulator-to-metal transition coupled with an anti-ferroelectric-to-paraelectric phase transition. The electronic structures of isostructural analogues, GeHfO_2 and SnHfO_2 , are also studied. We conclude the the 2D triangular lattice may serve as a complimentary platform to design new Xenics with diverse properties and functions.

II. COMPUTATIONAL METHODS

First-principles calculations are carried out with density functional theory (DFT) using the projector augmented wave (PAW) method implemented in the Vienna Ab initio Simulation (VASP) package^{50,51}. The energy cutoff of the plane wave basis set is 760 eV, and a $10 \times 16 \times 6$ Gamma-centered k -point mesh is used for Brillouin zone sampling. The lattice constants and atomic positions are fully optimized until the residual force on each atom is less than 0.001 eV/Å. We carefully compared the optimized structures of PbHfO_2 using different exchange-correlation energy functionals: local density approximation (LDA)⁵², generalized gradient approximation (GGA) with the Perdew-Burke-Ernzerhof (PBE) parameterization⁵³, PBE with Grimme dispersion corrections (PBE-D3)⁵⁴, optB88-vdW, and optB86b-vdW⁵⁵⁻⁵⁹. We find that LDA, PBE-D3, optB88-vdW, and optB86b-vdW predict similar structural parameters whereas PBE strongly overestimates the lattice constants. Therefore, all first-principles calculations reported here are performed using LDA. To reveal the spinless nodal line in the momentum space, the energy gap between selected pair of bands is calculated within the tight-binding (TB) scheme using WannierTools⁶⁰. The maximum localized Wannier functions (MLWF) TB Hamiltonian with Pb-5 p orbitals as projectors is constructed with Wannier90 interfaced with VASP⁶¹. The Z_2 invariant for the flat Pb monolayer including the effects of SOC is computed by tracking the evolution of hybrid Wannier functions using Z2Pack⁶².

III. RESULTS AND DISCUSSIONS

A. Electronic structure of flat Pb triangular lattice

The free-standing triangular-lattice Pb monolayer has a hexagonal unit cell with an in-plane lattice constant of 3.18 Å (optimized without SOC, Fig. 1a). As all Pb atoms are coplanar, the mirror reflection symmetry with respect to the xy plane (\mathcal{M}_z) is a natural consequence. The computed band structure without SOC is presented in Fig. 1b. There are two crossing points emerging along the high-symmetry path of M– Γ –K near the Fermi level (E_F), implying a possible closed loop on the Fermi surface. Figure 1c shows the momentum distribution of gapless nodal points in the $k_z = 0$ plane, confirming a spinless Dirac nodal loop in the absence of SOC. To check whether the Dirac nodal loop is symmetry protected, we calculate the eigenvalues of \mathcal{M}_z for the two bands near E_F . It is found that the two bands have opposite \mathcal{M}_z parities as marked by +1 and –1 in Fig. 1b. The opposing \mathcal{M}_z parities indicate that the two bands belong to different irreducible representations (IRs) and will not hybridize to open a gap.

The flat Pb monolayer has both time reversal symmetry (\mathcal{T}) and inversion symmetry (\mathcal{P}). In the presence of SOC and combined symmetry \mathcal{PT} , each band is doubly degenerate. Moreover, the Kramers pair will have opposing \mathcal{M}_z parities. This can be seen from $\mathcal{M}_z\mathcal{PT}\psi_+ = \mathcal{PT}\mathcal{M}_z\psi_+ = \mathcal{PT}i\psi_+ = -i\mathcal{PT}\psi_+$, which implies the Kramers pair ψ_+ and $\mathcal{PT}\psi_+$ have opposite mirror eigenvalues ($+i$ and $-i$). As a result, the two doublet Bloch states forming the nodal loop in the mirror invariant plane ($k_z = 0$) will hybridize and anticross. As shown in the band structure computed with SOC (Fig. 1d), the bands along M– Γ –K–M are fully gapped. Because of the large SOC strength afforded by Pb atoms, the size of SOC gap is quite large (≈ 1.1 eV). Similar to previous study of free-standing Cu_2Si where mirror-protected Dirac nodal lines are gapped after including SOC⁴⁶, here we also see the annihilation of Dirac nodal line in the presence of SOC. We calculate the Z_2 topological number and find that the flat Pb monolayer is a trivial semimetal (0:000) with an electron pocket around the high-symmetry point K (Fig. 1d).

B. Electronic structure of buckled Pb triangular lattice

It is well known that the atomic buckling can strongly affect the physical and chemical properties of 2D materials⁶³. We investigate the electronic structures of buckled Pb monolayer in which one column of Pb atoms (Pb1, colored in red) are shifted upwards while adjacent columns of Pb atoms (Pb2, colored in blue) are shifted downwards (Fig. 2a). This buckling pattern resembles 2D boron sheets grown on silver surfaces³⁹. The primitive unit cell of the buckled sheet contains two Pb atoms and has an orthorhombic lattice in the space group of $Pmmn$ ($a = 5.41$ Å and $b = 3.18$ Å, optimized without SOC). The parameter δ that measures the degree of buckling is defined as $\delta = \frac{1}{2}(z^{\text{Pb1}} - z^{\text{Pb2}})$ where z^{Pb} is the z -component of Pb position. One might expect the spinless nodal loop observed in the flat configuration would become gapped after the removal of the mirror reflection symmetry \mathcal{M}_z due to buckling. Interestingly, we identify a gapless nodal loop in buckled Pb monolayer ($\delta = 0.35$ Å) as well. The orbital-resolved band structure reveals Dirac-cone-like linear crossing points along high-symmetry lines of Γ –X and Γ –Y near E_F (Fig. 2b), corresponding to an anisotropic Dirac nodal loop in the $k_z = 0$ plane (Fig. 2c). This implies the existence of some symmetry other than \mathcal{M}_z ensuring gapless crossing at any arbitrary k -points lying in the plane of $k_z = 0$. It turns out the space group $Pmmn$ has a glide mirror plane $\{\mathcal{G}_z | \frac{1}{2}\frac{1}{2}\}$, which can also host nodal lines in glide-invariant planes in the momentum space.

Similar to the flat monolayer, the nodal line becomes fully gapped in the buckled Pb sheet after including SOC. This can be understood by following the analysis in the work of Fang *et al*⁶⁴. For a spinfull system, the bands in the glide-invariant plane $k_z = 0$ can be labeled by their \mathcal{G}_z eigenvalues $g_{\pm} = \pm ie^{i(k_x + k_y)/2}$. In the presence of \mathcal{PT} , all bands are two-fold degenerate at every k -point. Suppose at $(k_x, k_y, 0)$, ψ_+ satisfies $\mathcal{G}_z \psi_+ = g_+ \psi_+$, then $\mathcal{G}_z \mathcal{PT} \psi_+ = e^{i(k_x + k_y)} \mathcal{PT} \mathcal{G}_z \psi_+ = e^{i(k_x + k_y)} \mathcal{PT} i e^{i(k_x + k_y)/2} \psi_+ = g_- \mathcal{PT} \psi_+$, which implies the doubly-degenerate bands related by \mathcal{PT} form a Kramers pair while having opposite \mathcal{G}_z eigenvalues in the $k_z = 0$ plane. Therefore, the bands forming the nodal line are allowed to hybridize and open a gap when the SOC is considered (Fig. 2d). We find that the buckled Pb monolayer is a semiconductor with a band gap of 0.3 eV. Noted that all bands are four-fold degenerate at X, Y, and S, which are Dirac points protected by two screw axes $\{\mathcal{C}_x | \frac{1}{2}0\}$ and $\{\mathcal{C}_y | 0\frac{1}{2}\}$ ⁶⁵. In principle, one may tune the Fermi level (via hole or electron doping) to expose these Dirac points, making the system a 2D Dirac semimetal.

The finding that the flat Pb triangular lattice is a semimetal whereas its buckled sheet is a semiconductor suggests a metal-to-insulator transition driven by the atomic buckling. We calculate the energies and band gaps of Pb monolayer for different combinations of in-plane strains (η) and buckling parameters using an orthorhombic unit cell ($a = \sqrt{3}b$). The in-plane strain is defined as $\eta = (b - b_0)/b_0$, where b_0 is the equilibrium Pb-Pb distance in the flat monolayer. As expected, a compressive strain will favor a buckled configuration while a tensile strain will stabilize the flat configuration (Fig. 3a). From the calculated band gaps shown in Fig. 3b, it is clear that the band gap depends sensitively on the degree of buckling, and an insulator-to-metal transition can be realized by applying tensile strains. These results indicate the Pb monolayer allows for great tunability of the electronic properties via strain engineering. Moreover, we compute the energy difference between the Dirac point at X point (Fig. 2d) and the Fermi level (Fig. 3c) and find that the Dirac point is approaching the Fermi surface with increasing in-plane tensile strains.

C. Electronic structures of Ge and Sn triangular lattices

Figure 4 reports the optimized structures and electronic band structures for flat and buckled Ge and Sn triangular lattices. The band dispersions of flat Ge and Sn monolayers obtained without SOC closely resemble those in the flat Pb sheet, both indicating the presence of spinless nodal loops in the $k_z = 0$ plane. Similarly, buckled Ge and Sn monolayers also host nodal lines in glide-invariant planes in the momentum space, respectively. After considering SOC, the nodal lines become gapped. Because of the weak SOC strengths of Ge and Sn atoms, their buckled sheets show the features of semimetals, different from the semiconducting behavior of a buckled Pb triangular lattice. As the gaps at the anti-crossing points near E_F are relatively small and band dispersions remain largely linear, these two systems may act as 2D quasi-free-fermions in practice^{46,66}.

D. Design 3D materials supporting Pb monolayer

So far, we have treated group-IV triangular lattices as generic model systems. It is natural to ask whether it is feasible to access their tunable electronic structures in realistic materials. Our phonon calculations of the Pb monolayer reveal vibrational modes with imaginary

frequencies, indicating it is dynamically unstable. We propose to realize a quasi-3D material by stacking Pb triangular lattice with other “electrically inert” 2D materials in which the interlayer coupling is weak. With this design principle, we identify 1T-HfO₂ monolayer⁶⁷ as a suitable building block due to its wide band gap (6.73 eV) and lattice symmetry compatible with a triangular lattice. Similar to 2D transition metal dichalcogenides, the 1T-HfO₂ monolayer has two layers of hexagonal oxygen lattices sandwiching a slab of hexagonally packed Hf lattice, and each atomic layer has a triangular lattice symmetry. By alternately stacking Pb and 1T-HfO₂ monolayers, we obtain a quasi-3D material PbHfO₂. Figure 5a shows the optimized unit cell of PbHfO₂ which has a monoclinic space group $P2_1/m$ and lattice constants of $a = 5.492 \text{ \AA}$, $b = 3.187 \text{ \AA}$, $c = 9.118 \text{ \AA}$, $\beta = 96.7^\circ$, $\alpha = \gamma = 90^\circ$. The bucking parameter δ of the Pb layer in PbHfO₂ is 0.6 \AA . Interestingly, PbHfO₂ is antiferroelectric as Hf atoms are displaced with respect to the center of their surrounding oxygen octahedra while the two Hf atoms in the unit cell have opposite local displacements (Fig. 5a). The structure of PbHfO₂ is confirmed stable through computations of the phonon dispersions along high-symmetry lines of the Brillouin zone of the monoclinic unit cell (Fig. 5b). As shown in Fig. 5c, the phonon spectrum has no imaginary frequencies, demonstrating the designed material PbHfO₂ is indeed dynamically stable. Additionally, the dispersions along high-symmetry lines along k_z such as Γ –Y, A–M₁, X–H₁, and Z–D are nearly flat, indicating weak interactions between Pb and HfO₂ layers.

The electronic band structure and projected density of states (DOS) of PbHfO₂ in the absence of SOC are depicted in Fig. 5d. To compare directly with the band structure of a freestanding Pb monolayer, we plot the band dispersions along high-symmetry lines of the Brillouin zone of the primitive orthorhombic lattice. Clearly, the band dispersions near E_F bare strong similarity to those in the buckled Pb sheet (Fig. 2b). We find that the states close to the Fermi level are mainly from Pb-5*p* orbitals with negligible contributions from Hf and O atoms, supporting our design principle that the HfO₂ layer is “electrically inert”. The most notable change in the band structure of PbHfO₂ is the anti-crossing along Γ –X and Γ –Y (Fig. 5d). This is expected given that the $P2_1/m$ space group no longer hosts the mirror (\mathcal{M}_z) or the glide mirror (\mathcal{G}_z) symmetry. After considering SOC, PbHfO₂ is a semiconductor with a band gap of 0.14 eV (Fig. 5e). We add that the $P2_1/m$ space group still has a screw axis $\{\mathcal{C}_y|0\frac{1}{2}\}$, which protects the four-fold degenerate Dirac points at Y and S. However, these Dirac points are quite far away from the Fermi level, making it difficult

to access their topological properties.

E. Strain engineering of PbHfO₂

Advances in thin-film epitaxy taking advantage of misfit strains between the film and the underlying substrate have been widely used to finely control the structure, response, and properties of functional materials such as ferroelectrics^{68–70}, topological quantum materials^{71,72}, and low-dimensional materials^{73–75}. Our previous analysis of Pb monolayer has already shown that the band gaps depend strongly on the degree of buckling, which can be tuned by applying epitaxial strains.

We investigate the effects of in-plane deformations along the a and b axes by rescaling the lattice vectors of PbHfO₂ while allowing the atomic positions and the length of c axis to fully relax (the optimized structure is denoted as b-PbHfO₂). At each in-plane strain condition, we also carry out a constrained optimization of PbHfO₂ by forcing Pb atoms coplanar, denoted as f-PbHfO₂ (see illustration in Fig. 6a). This allows the determination of the stability of b-PbHfO₂ with a buckled Pb layer relative to f-PbHfO₂ as well as the critical strain at which a buckled-to-flat transition may occur. Figure 6a reports the evolution of the energies of b-PbHfO₂ and f-PbHfO₂ (E_b vs E_f), band gap (E_g), and local displacement of Hf ($d_z(\text{Hf})$) as a function of in-plane strains. It is found that at a critical tensile strain of $\approx 2\%$, the energies of b-PbHfO₂ and f-PbHfO₂ are nearly identical, and the system becomes metallic in both configurations. This strain-driven insulator-metal transition is coupled with an antiferroelectric-paraelectric phase transition as $d_z(\text{Hf})$ decreases with increasing tensile strains. We show the SOC band structures of b-PbHfO₂ and f-PbHfO₂ at some selective strain states in Fig. 6b-d.

F. Electronic structure of SnHfO₂

The isostructural analogues of PbHfO₂ are studied by replacing Pb with Ge and Sn, respectively. Due to the large lattice mismatch between HfO₂ and Ge monolayers, Ge atoms in the optimized GeHfO₂ form isolated 1D-channels. In comparison, the Sn atoms in SnHfO₂ are nearly coplanar and are arranged in a triangular lattice (Fig. 7a). The band structure in the scalar-relativistic case reveals multiple points resembling Dirac crossings along Y– Γ –X–S and Z–U–R–T (Fig. 7b). However, because SnHfO₂ is in the space group

of $P2_1/m$ which does not contain \mathcal{M}_z or \mathcal{G}_z , close examinations show that the topmost valence and the lowest conduction bands of SnHfO_2 are already gaped. The flat bands along $\Gamma-Z$ again confirm weak interactions between Sn and HfO_2 layers. When the SOC is taken into account, the electronic spectrum of SnHfO_2 further gaps out (Fig. 7c). The four-fold degeneracy at Y and S points remain protected due to the screw axis $\{\mathcal{C}_y|0\frac{1}{2}\}$.

IV. CONCLUSIONS

First-principle density functional theory calculations are employed to explore the structural and electronic properties of 2D triangular lattices made of group-IV elements. Unlike Xenes with a honeycomb symmetry, 2D monoelemental crystal with a triangular lattice is mostly overlooked by the mainstream research. This work aims to fill in the gap and to encourage further experimental and theoretical studies on this new type of broadly-defined Xene. Our results demonstrate that these 2D triangular lattices may host rich physics, ranging from nonsymmorphic-symmetry-protected nodal lines and Dirac points to strain-driven metal-insulator transitions. The designed quasi-3D crystal PbHfO_2 is predicted to be dynamically stable and largely retains the electronic properties of 2D Pb triangular lattice. The emergence of anti-ferroelectricity in PbHfO_2 opens up opportunities for electric field-control of the buckling of Pb monolayer and its band gaps. The design principle proposed here to alternatively stacking electrically inert HfO_2 monolayer and 2D Pb/Sn monolayers can also be applied to known Xenes such as stanene and plumbene, offering a useful platform to design and manipulate emergent phenomena in Xenes.

V. ACKNOWLEDGMENTS

XD and SL acknowledge the support from Westlake Foundation. The computational resource is provided by Westlake Supercomputer Center.

* liushi@westlake.edu.cn

¹ M. Houssa, A. Dimoulas, and A. Molle, *2D materials for nanoelectronics*, Vol. 17 (CRC Press, 2016).

- ² R. Mas-Balleste, C. Gomez-Navarro, J. Gomez-Herrero, and F. Zamora, 2D materials: to graphene and beyond, *Nanoscale* **3**, 20 (2011).
- ³ M. Chhowalla, D. Jena, and H. Zhang, Two-dimensional semiconductors for transistors, *Nat. Rev. Mater.* **1**, 16052 (2016).
- ⁴ I. Brihuega, P. Mallet, H. González-Herrero, G. Trambly de Laissardière, M. M. Ugeda, L. Magaud, J. M. Gómez-Rodríguez, F. Ynduráin, and J.-Y. Veullen, Unraveling the intrinsic and robust nature of van hove singularities in twisted bilayer graphene by scanning tunneling microscopy and theoretical analysis, *Phys. Rev. Lett.* **109**, 196802 (2012).
- ⁵ A. K. Geim and I. V. Grigorieva, Van der waals heterostructures, *Nature* **499**, 419 (2013).
- ⁶ K. Novoselov, A. Mishchenko, A. Carvalho, and A. C. Neto, 2D materials and van der waals heterostructures, *Science* **353** (2016).
- ⁷ Y. Liu, N. O. Weiss, X. Duan, H.-C. Cheng, Y. Huang, and X. Duan, Van der waals heterostructures and devices, *Nat. Rev. Mater.* **1**, 1 (2016).
- ⁸ Y. Cao, V. Fatemi, S. Fang, K. Watanabe, T. Taniguchi, E. Kaxiras, and P. Jarillo-Herrero, Unconventional superconductivity in magic-angle graphene superlattices, *Nature* **556**, 43 (2018).
- ⁹ K. S. Novoselov, Electric field effect in atomically thin carbon films, *Science* **306**, 666 (2004).
- ¹⁰ K. S. Novoselov, D. Jiang, F. Schedin, T. Booth, V. Khotkevich, S. Morozov, and A. K. Geim, Two-dimensional atomic crystals, *PNAS* **102**, 10451 (2005).
- ¹¹ E. P. Randviir, D. A. Brownson, and C. E. Banks, A decade of graphene research: production, applications and outlook, *Mater. Today* **17**, 426 (2014).
- ¹² P. Bridgman, Two new modifications of phosphorus, *J. Am. Chem. Soc.* **36**, 1344 (1914).
- ¹³ B. Radisavljevic, A. Radenovic, J. Brivio, V. Giacometti, and A. Kis, Single-layer MoS₂ transistors, *Nat. Nanotechnology* **6**, 147 (2011).
- ¹⁴ L. Liu, Y. P. Feng, and Z. X. Shen, Structural and electronic properties of h-BN, *Phys. Rev. B* **68**, 104102 (2003).
- ¹⁵ J. Memon, J. Sun, D. Meng, W. Ouyang, M. A. Memon, Y. Huang, S. Yan, and J. Geng, Synthesis of graphene/Ni–Al layered double hydroxide nanowires and their application as an electrode material for supercapacitors, *J. Mater. Chem.A* **2**, 5060 (2014).
- ¹⁶ S. Saha, M. Jana, P. Khanra, P. Samanta, H. Koo, N. C. Murmu, and T. Kuila, Band gap engineering of boron nitride by graphene and its application as positive electrode material in asymmetric supercapacitor device, *ACS Appl. Mater. Interfaces* **7**, 14211 (2015).

- ¹⁷ S. Wu, K. S. Hui, and K. N. Hui, 2D black phosphorus: from preparation to applications for electrochemical energy storage, *Adv. Sci.* **5**, 1700491 (2018).
- ¹⁸ P. Joensen, R. Frindt, and S. R. Morrison, Single-layer MoS₂, *Mater. Res. Bull.* **21**, 457 (1986).
- ¹⁹ K. Choudhary, I. Kalish, R. Beams, and F. Tavazza, High-throughput identification and characterization of two-dimensional materials using density functional theory, *Sci. Rep.* **7**, 5179 (2017).
- ²⁰ N. Mounet, M. Gibertini, P. Schwaller, D. Campi, A. Merkys, A. Marrazzo, T. Sohier, I. E. Castelli, A. Cepellotti, G. Pizzi, *et al.*, Two-dimensional materials from high-throughput computational exfoliation of experimentally known compounds, *Nat. Nanotechnology* **13**, 246 (2018).
- ²¹ T. Roy, M. Tosun, J. S. Kang, A. B. Sachid, S. B. Desai, M. Hettick, C. C. Hu, and A. Javey, Field-effect transistors built from all two-dimensional material components, *ACS Nano* **8**, 6259 (2014).
- ²² C. Grazianetti, C. Martella, and A. Molle, The xenes generations: A taxonomy of epitaxial single-element 2D materials, *Phys. Status Solidi RRL* **14**, 1900439 (2020).
- ²³ P. Vogt, P. De Padova, C. Quaresima, J. Avila, E. Frantzeskakis, M. C. Asensio, A. Resta, B. Ealet, and G. Le Lay, Silicene: Compelling experimental evidence for graphenelike two-dimensional silicon, *Phys. Rev. Lett.* **108**, 155501 (2012).
- ²⁴ A. Kara, H. Enriquez, A. P. Seitsonen, L. L. Y. Voon, S. Vizzini, B. Aufray, and H. Oughaddou, A review on silicene new candidate for electronics, *Surf. Sci. Rep.* **67**, 1 (2012).
- ²⁵ L. Tao, E. Cinquanta, D. Chiappe, C. Grazianetti, M. Fanciulli, M. Dubey, A. Molle, and D. Akincinwande, Silicene field-effect transistors operating at room temperature, *Nat. Nanotechnology* **10**, 227 (2015).
- ²⁶ S. Salahuddin, K. Ni, and S. Datta, The era of hyper-scaling in electronics, *Nat. Electron.* **1**, 442 (2018).
- ²⁷ C. L. Kane and E. J. Mele, Quantum spin hall effect in graphene, *Phys. Rev. Lett.* **95**, 226801 (2005).
- ²⁸ Y. Yao, F. Ye, X.-L. Qi, S.-C. Zhang, and Z. Fang, Spin-orbit gap of graphene: First-principles calculations, *Phys. Rev. B* **75**, 041401 (2007).
- ²⁹ M. Ezawa, Monolayer topological insulators: Silicene, germanene, and stanene, *J. Phys. Soc. Jpn.* **84**, 121003 (2015).

- ³⁰ C.-L. Lin, R. Arafune, K. Kawahara, N. Tsukahara, E. Minamitani, Y. Kim, N. Takagi, and M. Kawai, Structure of silicene grown on Ag(111), *Appl. Phys. Express* **5**, 045802 (2012).
- ³¹ M. E. Dávila, L. Xian, S. Cahangirov, A. Rubio, and G. L. Lay, Germanene: a novel two-dimensional germanium allotrope akin to graphene and silicene, *New J. Phys.* **16**, 095002 (2014).
- ³² A. Acun, L. Zhang, P. Bampoulis, M. Farmanbar, A. van Houselt, A. Rudenko, M. Lingenfelder, G. Brocks, B. Poelsema, M. Katsnelson, *et al.*, Germanene: the germanium analogue of graphene, *J. Phys.: Condens. Matter* **27**, 443002 (2015).
- ³³ F. feng Zhu, W. jiong Chen, Y. Xu, C. lei Gao, D. dan Guan, C. hua Liu, D. Qian, S.-C. Zhang, and J. feng Jia, Epitaxial growth of two-dimensional stanene, *Nat. Mater.* **14**, 1020 (2015).
- ³⁴ J. Yuhara, B. He, N. Matsunami, M. Nakatake, and G. L. Lay, Graphene’s latest cousin: Plumbene epitaxial growth on a “Nano WaterCube”, *Adv. Mater.* **31**, 1901017 (2019).
- ³⁵ S. Balendhran, S. Walia, H. Nili, S. Sriram, and M. Bhaskaran, Elemental analogues of graphene: silicene, germanene, stanene, and phosphorene, *Small* **11**, 640 (2015).
- ³⁶ H. Zhao, C.-w. Zhang, W.-x. Ji, R.-w. Zhang, S.-s. Li, S.-s. Yan, B.-m. Zhang, P. Li, and P.-j. Wang, Unexpected giant-gap quantum spin hall insulator in chemically decorated plumbene monolayer, *Sci. Rep.* **6**, 1 (2016).
- ³⁷ Z.-Q. Huang, C.-H. Hsu, F.-C. Chuang, Y.-T. Liu, H. Lin, W.-S. Su, V. Ozolins, and A. Bansil, Strain driven topological phase transitions in atomically thin films of group IV and V elements in the honeycomb structures, *New J. Phys.* **16**, 105018 (2014).
- ³⁸ X.-L. Yu, L. Huang, and J. Wu, From a normal insulator to a topological insulator in plumbene, *Phys. Rev. B* **95**, 125113 (2017).
- ³⁹ A. J. Mannix, X.-F. Zhou, B. Kiraly, J. D. Wood, D. Alducin, B. D. Myers, X. Liu, B. L. Fisher, U. Santiago, J. R. Guest, M. J. Yacaman, A. Ponce, A. R. Oganov, M. C. Hersam, and N. P. Guisinger, Synthesis of borophenes: Anisotropic, two-dimensional boron polymorphs, *Science* **350**, 1513 (2015).
- ⁴⁰ B. Feng, J. Zhang, Q. Zhong, W. Li, S. Li, H. Li, P. Cheng, S. Meng, L. Chen, and K. Wu, Experimental realization of two-dimensional boron sheets, *Nat. Chem.* **8**, 563 (2016).
- ⁴¹ J. L. Zhang, S. Zhao, C. Han, Z. Wang, S. Zhong, S. Sun, R. Guo, X. Zhou, C. D. Gu, K. D. Yuan, Z. Li, and W. Chen, Epitaxial growth of single layer blue phosphorus: A new phase of two-dimensional phosphorus, *Nano Lett.* **16**, 4903 (2016).

- ⁴² F. Reis, G. Li, L. Dudy, M. Bauernfeind, S. Glass, W. Hanke, R. Thomale, J. Schäfer, and R. Claessen, Bismuthene on a SiC substrate: A candidate for a high-temperature quantum spin hall material, *Science* **357**, 287 (2017).
- ⁴³ V. Kochat, A. Samanta, Y. Zhang, S. Bhowmick, P. Manimunda, S. A. S. Asif, A. S. Stender, R. Vajtai, A. K. Singh, C. S. Tiwary, and P. M. Ajayan, Atomically thin gallium layers from solid-melt exfoliation, *Sci. Adv.* **4**, e1701373 (2018).
- ⁴⁴ S. M. Beladi-Mousavi, A. M. Pourrahimi, Z. Sofer, and M. Pumera, Atomically thin 2D-arsenene by liquid-phased exfoliation: Toward selective vapor sensing, *Adv. Funct. Mater.* , 1807004 (2018).
- ⁴⁵ J. Zhang, B. Zhao, Y. Xue, T. Zhou, and Z. Yang, Coupling effect of topological states and Chern insulators in two-dimensional triangular lattices, *Phys. Rev. B* **97**, 125430 (2018).
- ⁴⁶ B. Feng, B. Fu, S. Kasamatsu, S. Ito, P. Cheng, C.-C. Liu, Y. Feng, S. Wu, S. K. Mahatha, P. Sheverdyaeva, *et al.*, Experimental realization of two-dimensional dirac nodal line fermions in monolayer Cu₂Si, *Nat. Commun.* **8**, 1007 (2017).
- ⁴⁷ G. Bian, T.-R. Chang, R. Sankar, S.-Y. Xu, H. Zheng, T. Neupert, C.-K. Chiu, S.-M. Huang, G. Chang, I. Belopolski, *et al.*, Topological nodal-line fermions in spin-orbit metal PbTaSe₂, *Nat. Commun.* **7**, 10556 (2016).
- ⁴⁸ T. Zhang, P. Cheng, W.-J. Li, Y.-J. Sun, G. Wang, X.-G. Zhu, K. He, L. Wang, X. Ma, X. Chen, *et al.*, Superconductivity in one-atomic-layer metal films grown on Si (111), *Nat. Phys.* **6**, 104 (2010).
- ⁴⁹ J. Noffsinger and M. L. Cohen, Superconductivity in monolayer Pb on Si (111) from first principles, *Solid State Commun.* **151**, 421 (2011).
- ⁵⁰ P. E. Blochl, Projector augmented-wave method, *Phys. Rev. B* **50**, 17953 (1994).
- ⁵¹ G. Kresse and F. J. J, Efficient iterative schemes for ab initio total-energy calculations using a plane-wave basis set, *Phys. Rev. B* **54**, 11169 (1996).
- ⁵² J. P. Perdew and A. Zunger, Self-interaction correction to density-functional approximations for many-electron systems, *Phys. Rev. B* **23**, 5048 (1981).
- ⁵³ J. P. Perdew, K. Burke, and M. Ernzerhof, Generalized gradient approximation made simple, *Phys. Rev. Lett.* **77**, 3865 (1996).
- ⁵⁴ S. Grimme, J. Antony, S. Ehrlich, and H. Krieg, A consistent and accurate ab initio parametrization of density functional dispersion correction (DFT-D) for the 94 elements H-Pu, *J. Chem.*

- Phys. **132**, 154104 (2010).
- ⁵⁵ M. Dion, H. Rydberg, E. Schröder, D. C. Langreth, and B. I. Lundqvist, Van der waals density functional for general geometries, Phys. Rev. Lett. **92** (2004).
 - ⁵⁶ G. Román-Pérez and J. M. Soler, Efficient implementation of a van der waals density functional: Application to double-wall carbon nanotubes, Phys. Rev. Lett. **103** (2009).
 - ⁵⁷ T. Thonhauser, V. R. Cooper, S. Li, A. Puzder, P. Hyldgaard, and D. C. Langreth, Van der waals density functional: Self-consistent potential and the nature of the van der waals bond, Phys. Rev. B **76** (2007).
 - ⁵⁸ J. Klimeš, D. R. Bowler, and A. Michaelides, Chemical accuracy for the van der waals density functional, J. Phys.: Condens. Matter **22**, 022201 (2009).
 - ⁵⁹ J. Klimeš, D. R. Bowler, and A. Michaelides, Van der waals density functionals applied to solids, Phys. Rev. B **83** (2011).
 - ⁶⁰ Q. S. Wu, S. N. Zhang, H. F. Song, M. Troyer, and A. A. Soluyanov, Wanniertools: An open-source software package for novel topological materials, Comput. Phys. Commun. , S0010465517303442 (2017).
 - ⁶¹ N. Marzari and D. Vanderbilt, Maximally localized generalized wannier functions for composite energy bands, Phys. Rev. B **56**, 12847 (1997).
 - ⁶² D. Gresch, G. Autès, O. V. Yazyev, M. Troyer, D. Vanderbilt, B. A. Bernevig, and A. A. Soluyanov, Z2pack: Numerical implementation of hybrid wannier centers for identifying topological materials, Phys. Rev. B **95**, 075146 (2017).
 - ⁶³ A. Molle, J. Goldberger, M. Houssa, Y. Xu, S.-C. Zhang, and D. Akinwande, Buckled two-dimensional xene sheets, Nat. Mater. **16**, 163 (2017).
 - ⁶⁴ C. Fang, Y. Chen, H.-Y. Kee, and L. Fu, Topological nodal line semimetals with and without spin-orbital coupling, Phys. Rev. B **92**, 081201 (2015).
 - ⁶⁵ S. M. Young and C. L. Kane, Dirac semimetals in two dimensions, Phys. Rev. Lett. **115**, 126803 (2015).
 - ⁶⁶ Y.-J. Jin, R. Wang, J.-Z. Zhao, Y.-P. Du, C.-D. Zheng, L.-Y. Gan, J.-F. Liu, H. Xu, and S. Y. Tong, The prediction of a family group of two-dimensional node-line semimetals, Nanoscale **9**, 13112 (2017).
 - ⁶⁷ J. Weng and S.-P. Gao, A honeycomb-like monolayer of HfO₂ and the calculation of static dielectric constant eliminating the effect of vacuum spacing,

- Phys. Chem. Chem. Phys. **20**, 26453 (2018).
- ⁶⁸ D. G. Schlom, L. Q. Chen, C. B. Eom, K. M. Rabe, S. K. Streiffer, and J. M. Triscone, Strain tuning of ferroelectric thin films, *Ann. Rev. Mater. Res.* **37**, 589 (2007).
- ⁶⁹ A. R. Damodaran, J. C. Agar, S. Pandya, Z. Chen, L. Dedon, R. Xu, B. Apgar, S. Saremi, and L. W. Martin, New modalities of strain-control of ferroelectric thin films, *J. Phys.: Condens. Matter* **28**, 263001 (2016).
- ⁷⁰ R. Xu, S. Liu, I. Grinberg, J. Karthik, A. R. Damodaran, A. M. Rappe, and L. W. Martin, Ferroelectric polarization reversal via successive ferroelastic transitions, *Nat. Mater.* **14**, 79 (2015).
- ⁷¹ Y. Liu, Y. Y. Li, S. Rajput, D. Gilks, L. Lari, P. L. Galindo, M. Weinert, V. K. Lazarov, and L. Li, Tuning dirac states by strain in the topological insulator Bi_2Se_3 , *Nat. Phys.* **10**, 294 (2014).
- ⁷² S. Liu, Y. Kim, L. Z. Tan, and A. M. Rappe, Strain-induced ferroelectric topological insulator, *Nano Lett.* **16**, 1663 (2016).
- ⁷³ R. Xu, J. Huang, E. S. Barnard, S. S. Hong, P. Singh, E. K. Wong, T. Jansen, V. Harbola, J. Xiao, B. Y. Wang, S. Crossley, D. Lu, S. Liu, and H. Y. Hwang, Strain-induced room-temperature ferroelectricity in SrTiO_3 membranes, *Nat. Commun.* **11**, 3141 (2020).
- ⁷⁴ Z. Li, Y. Lv, L. Ren, J. Li, L. Kong, Y. Zeng, Q. Tao, R. Wu, H. Ma, B. Zhao, D. Wang, W. Dang, K. Chen, L. Liao, X. Duan, X. Duan, and Y. Liu, Efficient strain modulation of 2D materials via polymer encapsulation, *Nat. Commun.* **11**, 1151 (2020).
- ⁷⁵ C. Zhao, M. Hu, J. Qin, B. Xia, C. Liu, S. Wang, D. Guan, Y. Li, H. Zheng, J. Liu, and J. Jia, Strain tunable semimetal-topological-insulator transition in monolayer $1\text{-T}'\text{-WTe}_2$, *Phys. Rev. Lett.* **125**, 046801 (2020).

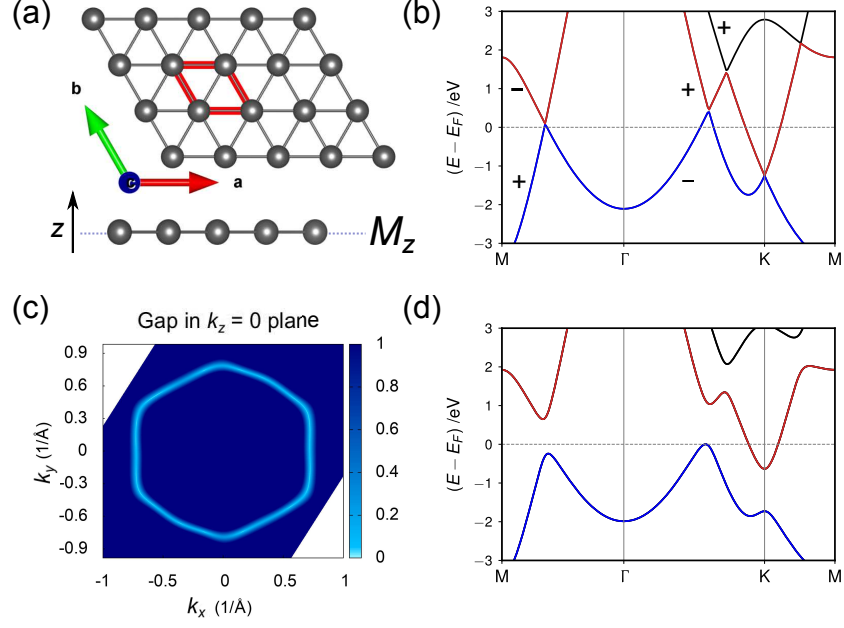


FIG. 1. Electronic structures of flat Pb triangular lattice. (a) Crystal structure of Pb triangular lattice with mirror symmetry \mathcal{M}_z . The 2D hexagonal unit cell is highlighted in red. (b) Electronic band structure without SOC along high-symmetry lines of the Brillouin zone of the hexagonal unit cell. (c) Spinless nodal loop in the $k_z = 0$ plane. (d) Electronic band structure with SOC. The topmost valence and lowest conduction band are colored in blue and red, respectively.

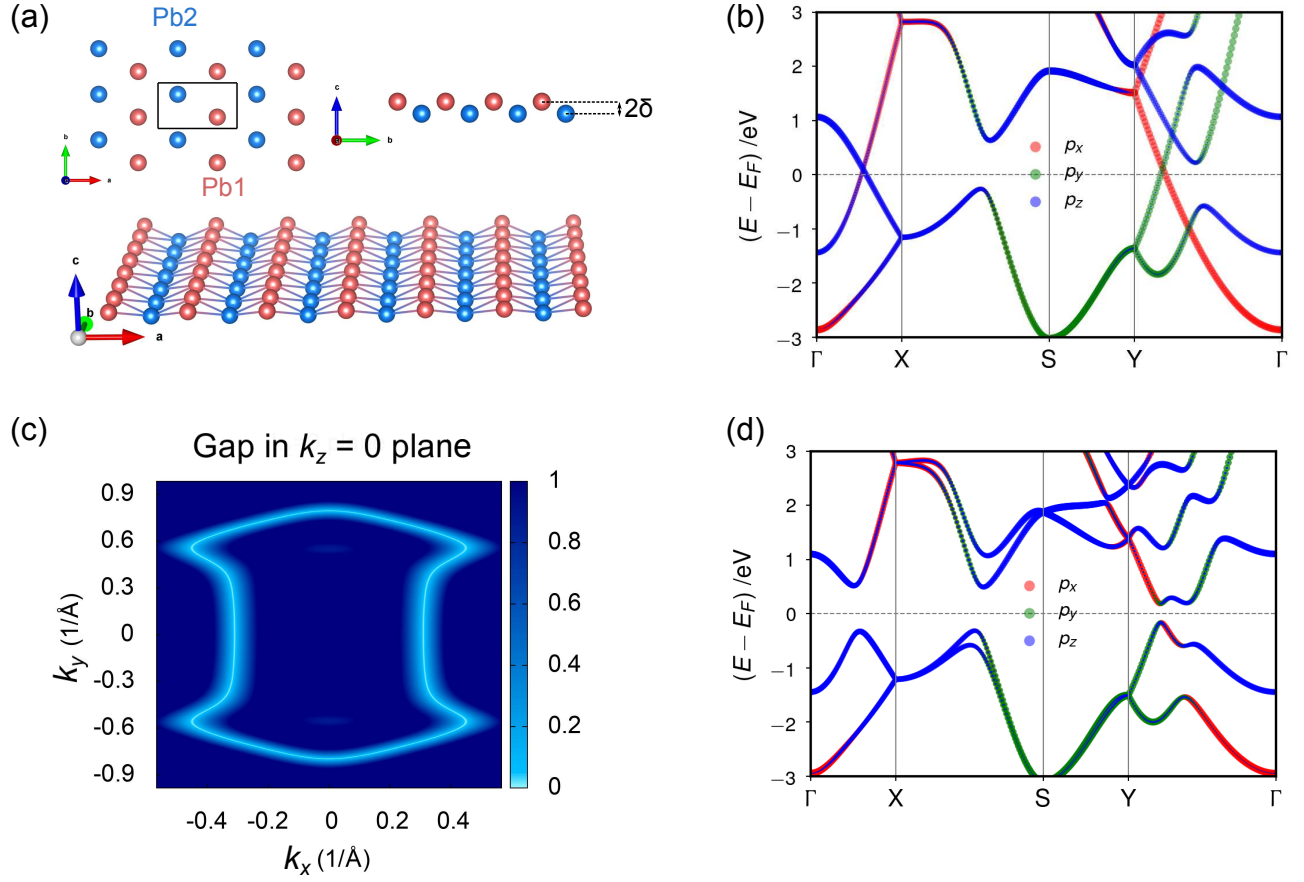


FIG. 2. Electronic structures of buckled Pb triangular lattice. (a) Crystal structure of buckled Pb sheet. The orthorhombic unit cell has two atoms colored in red and blue respectively. (b) Orbital-resolved electronic band structure without SOC along high-symmetry lines of the Brillouin zone of the orthorhombic unit cell. (c) Spinless nodal loop in the $k_z = 0$ plane. (d) Orbital-resolved band structure with SOC.

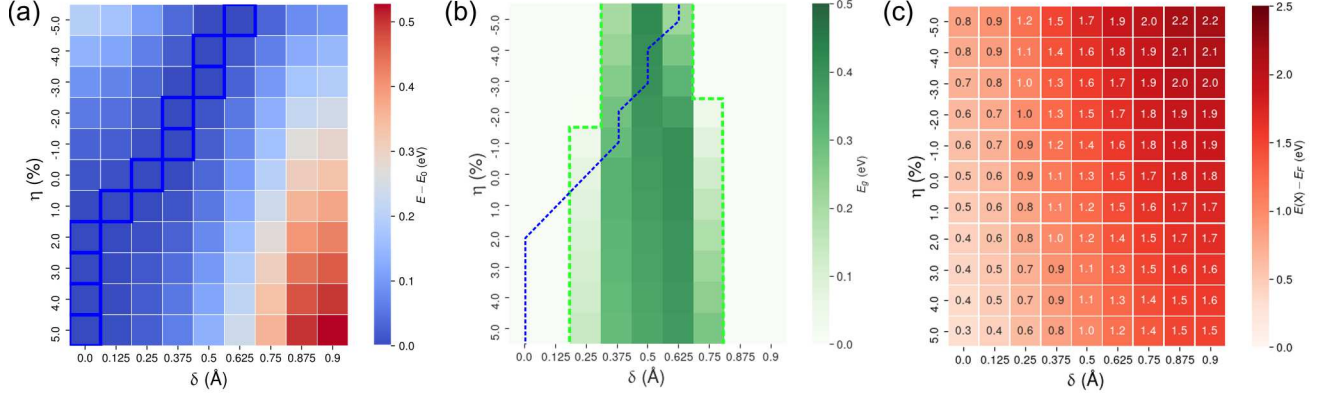


FIG. 3. Structural and electronic properties of Pb triangular lattice as a function of in-plane strains (η) and buckling parameters (δ). (a) Relative energies as a function of η and δ . At each in-plane strain state, the configuration with the lowest energy (E_0 , highlighted by a blue square) is chosen as the reference for the calculations of energy differences ($E - E_0$). (b) Band gaps (E_g) as a function of η and δ . The metal-insulator transition boundaries are highlighted by dashed lines in green. The dashed blue line tracks the lowest-energy configurations in (a), and reveals an insulator-to-metal transition with increasing tensile strains. (c) Energy difference between the four-fold degenerate Dirac point at the high-symmetry k -point X and the Fermi level (E_F) with respect to η and δ .

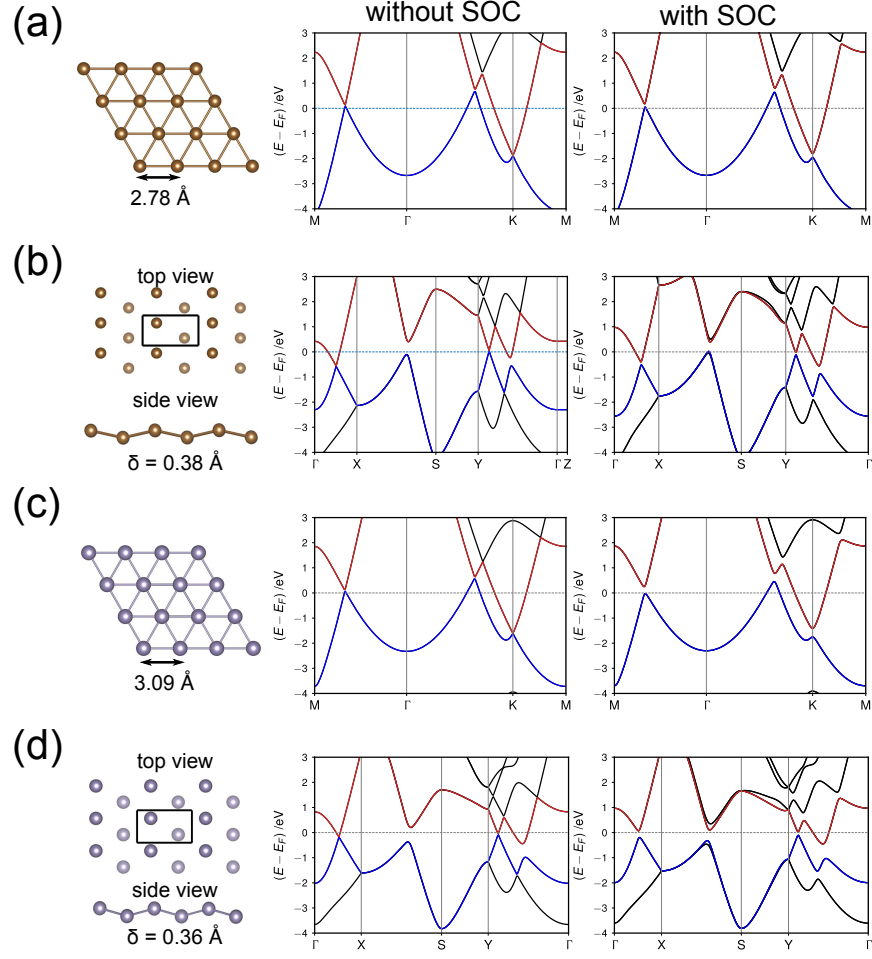


FIG. 4. Electronic band structures for (a) flat and (b) buckled Ge monolayer and (c) flat and (d) buckled Sn monolayer in a triangular lattice.

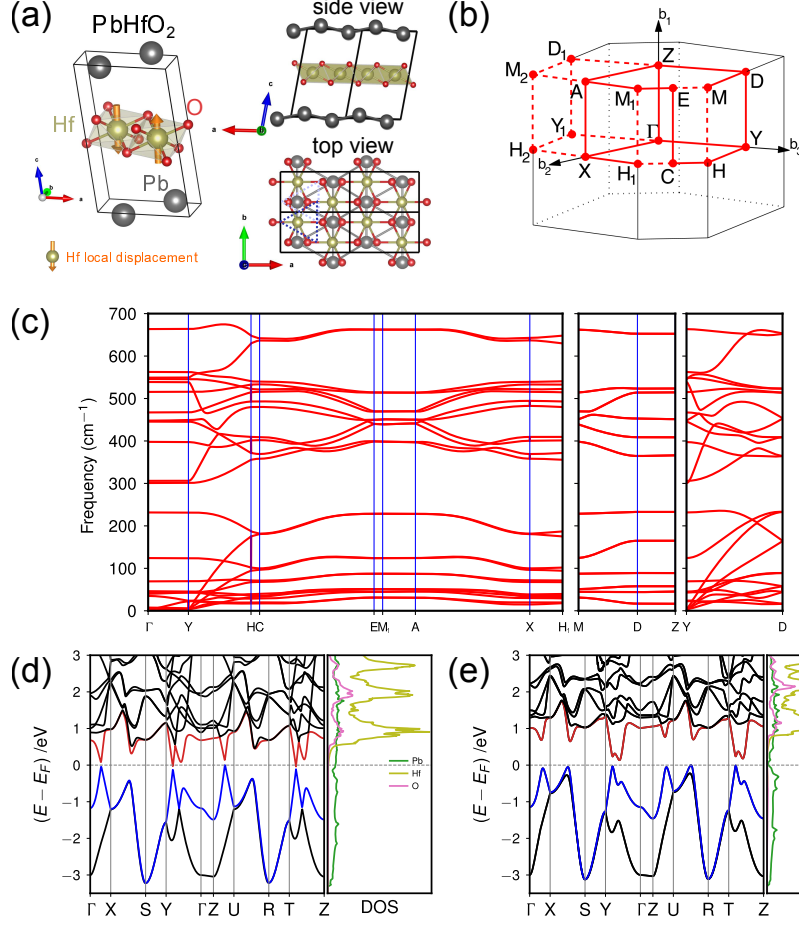


FIG. 5. Electronic structures of PbHfO_2 . (a) Crystal structure of PbHfO_2 in the space group of $P2_1/m$. (b) Brillouin zone of a monoclinic unit cell. (c) Phonon spectrum along high-symmetry lines of the Brillouin zone of the monoclinic unit cell. Electronic band structures and projected density of states (DOS) (d) without SOC and (e) with SOC. The topmost valence and lowest conduction band are colored in blue and red, respectively.

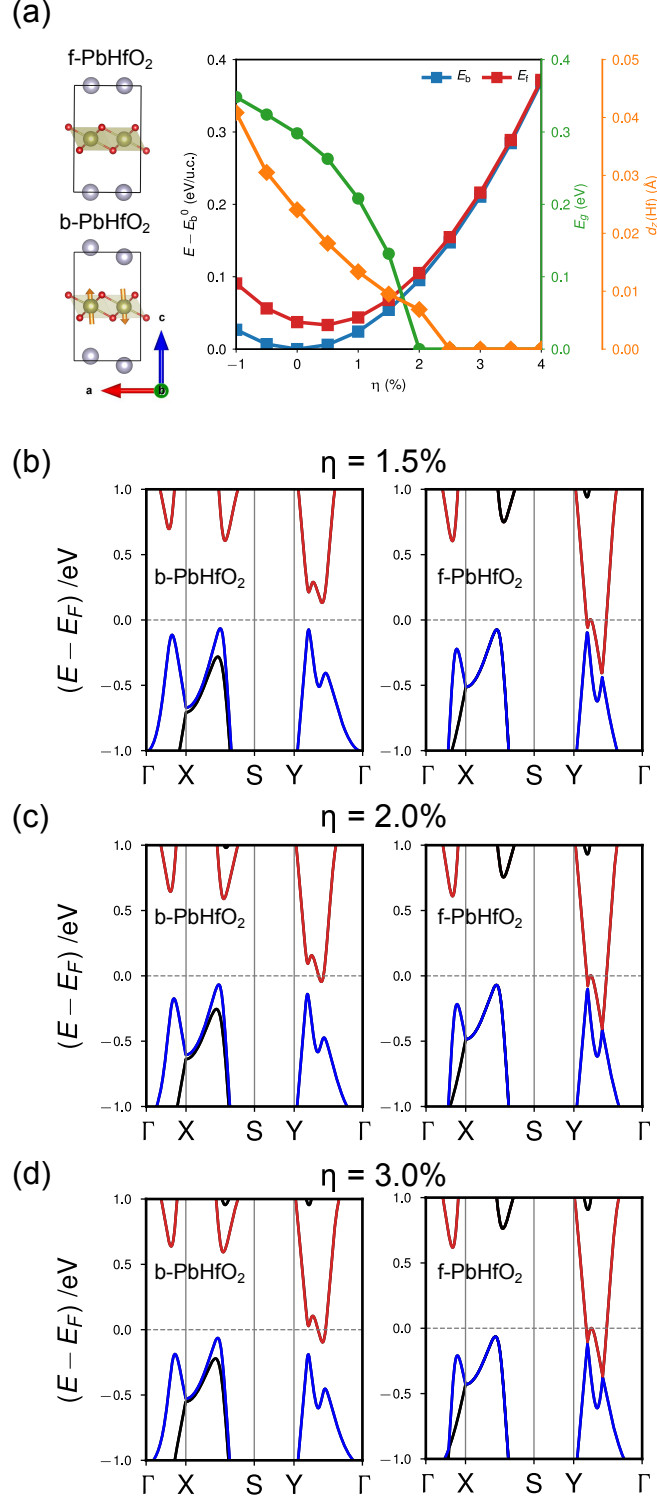


FIG. 6. (a) Evolution of energies, band gaps (E_g), and Hf local displacements ($d_z(\text{Hf})$) as a function of in-plane strains η . The energy of the ground state of PbHfO₂ (E_b^0) is chosen as the zero energy reference. E_b and E_f are the energies of b-PbHfO₂ and f-PbHfO₂, respectively. Band structures of b-PbHfO₂ (left) and f-PbHfO₂ (right) at (b) $\eta = 1.5\%$, (c) $\eta = 2.0\%$, and (d) $\eta = 3.0\%$

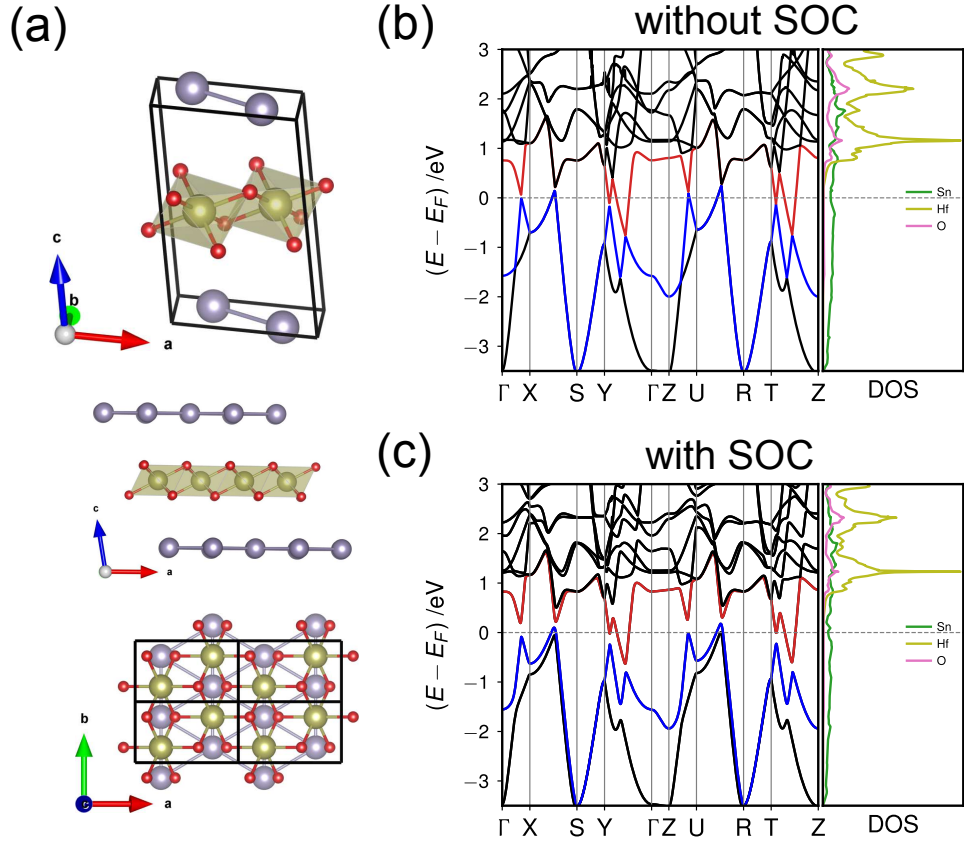


FIG. 7. Electronic structures of SnHfO₂. (a) Optimized structure of SnHfO₂ in the space group of $P2_1/m$. Electronic band structure (b) without SOC and (c) with SOC